Local Structural and Environmental Factors Define the Efficiency of an RNA Pseudoknot Involved in Programmed Ribosomal Frameshift Process

2 AUTHORS:

Asmita Gupta
Indian Institute of Science
2 PUBLICATIONS **0** CITATIONS

SEE PROFILE

Manju Bansal
Indian Institute of Science
113 PUBLICATIONS **2,776** CITATIONS

SEE PROFILE

Local Structural and Environmental Factors Define the Efficiency of an RNA Pseudoknot Involved in Programmed Ribosomal Frameshift Process

Asmita Gupta and Manju Bansal*

Molecular Biophysics Unit, Indian Institute of Science, Bangalore, Karnataka 560012, India

Ⓢ *Supporting Information*

ABSTRACT: In programmed −1 ribosomal frameshift, an RNA pseudoknot stalls the ribosome at specific sequence and restarts translation in a new reading frame. A precise understanding of structural characteristics of these pseudoknots and their PRF inducing ability has not been clear to date. To investigate this phenomenon, we have studied various structural aspects of a −1 PRF inducing RNA pseudoknot from BWYV using extensive molecular dynamics simulations. A set of functional and poorly functional forms, for which previous mutational data were available, were chosen for analysis. These structures differ from each other by either single base substitutions or base-pair replacements from the native structure. We have rationalized how certain mutations in RNA pseudoknot affect its function; e.g., a specific base substitution in loop 2 stabilizes the junction geometry by forming multiple noncanonical hydrogen bonds, leading to a highly rigid structure that could effectively resist ribosome-induced unfolding, thereby increasing efficiency. While, a CG to AU pair substitution in stem 1 leads to loss of noncanonical hydrogen bonds between stems and loop, resulting in a less stable structure and reduced PRF inducing ability, inversion of a pair in stem 2 alters specific base-pair geometry that might be required in ribosomal recognition of nucleobase groups, negatively affecting pseudoknot functioning. These observations illustrate that the ability of an RNA pseudoknot to induce −1 PRF with an optimal rate depends on several independent factors that contribute to either the local conformational variability or geometry.
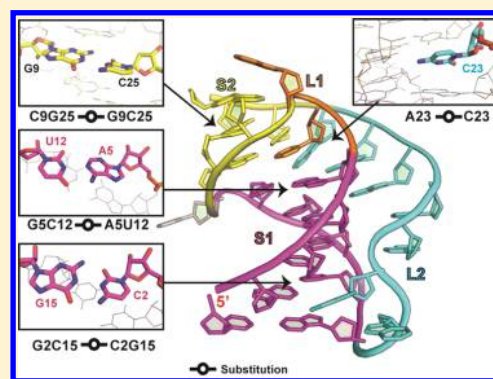
■ INTRODUCTION

RNA pseudoknots arguably present the best examples of the flexibility of an RNA chain and structural diversity arising due to it. An RNA pseudoknot is formed when unpaired residues present in the single-stranded loop regions of an RNA hairpin structure form complementary base pairs with unpaired residues located elsewhere in the RNA chain, giving rise to two helical stems interspersed by two loops.[1−4] They play a wide variety of roles in cellular processes, ranging from formation of catalytic core of ribozymes[1,5] to regulation of gene expression in a number of biological systems.[6−8] They are especially associated with the replication cycle of many single-stranded RNA viruses (ssRNA).[9,10] One of the most intriguing of these biological processes, mediated by an H-type or "classical" pseudoknot is the programmed −1 ribosomal frameshift (−1 PRF), a translational recoding event which maintains a precise ratio of structural to enzymatic proteins in a host of ssRNA viruses.[11,12] The efficiency of −1 PRF is determined by this ratio.[13] Apart from viruses, −1 PRF has also been identified in regulation of some prokaryotic and mammalian genes.[14−17]

The basic components of −1 PRF process comprise a 7-nucleotide long "slippery site" followed by a spacer region of 8−10 nucleotides long and an RNA pseudoknot or stem-loop. The role of this structure is mainly to act as a "roadblock"[18] for the actively translating ribosome and force it to shift its codon reading register by −1 nucleotide (Figure 1). The earliest model explaining the mechanism behind −1 PRF process, also known as the simultaneous slippage model,[19,20] proposed that both the P- and A-site codon bound tRNAs slip back toward 5′ direction, by −1 nucleotide from the current reading frame and maintain at least 2 codon−anticodon base pairs in the new shifted frame. Several studies either present this model in alternative perspectives[21] or support it with various chemical probing studies on downstream RNA structure or toeprinting studies involving pseudoknot/hairpin attenuated ribosome−RNA complexes.[22,23] Of particular interest among these investigations are those that attempt to link the efficiency of −1 PRF process to thermodynamic stability[24] or mechanical strength of the RNA pseudoknot structure.[25,26] With the advancement in crystallographic techniques, in recent years different theories other than the simultaneous slippage model have been developed to explain the precise molecular mechanism behind RNA pseudoknot-induced −1 PRF. These theories try to unlink the extent of ribosomal pausing on the downstream RNA structural element with the efficiency of −1
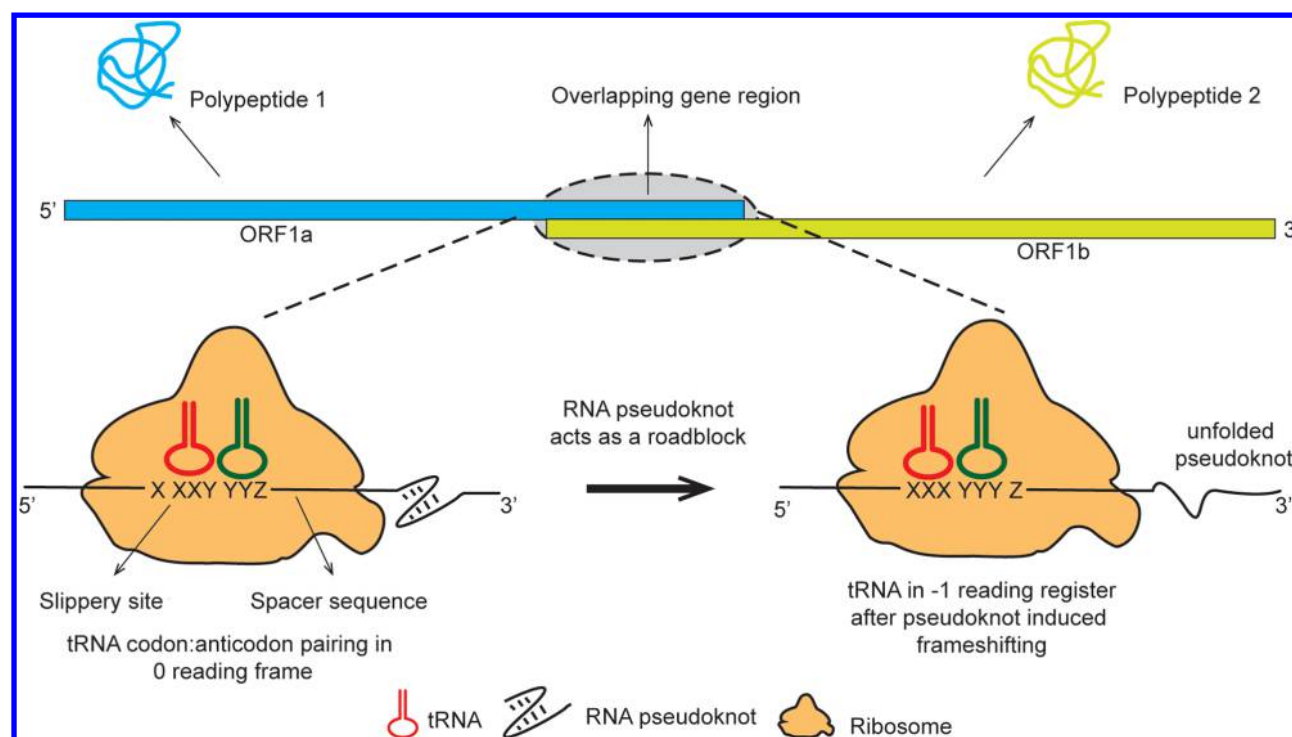
Figure 1. Schematic representation of programmed −1 ribosomal frameshifting. Major components of the process include an overlapping gene segment containing a "slippery site", spacer region, and RNA structure that blocks the ribosome during translation process. P-site and A-site tRNAs are shown in red and green colors, respectively.

PRF,[27] and thereby indicate the presence of additional structural contacts between ribosome and pseudoknot. Cryo-EM studies demonstrated the geometry of P- and A-site bound tRNAs in ribosome,[28] paused at a downstream RNA pseudoknot, and investigated the role of structural tension thus created in the mRNA codon bound tRNA structures. The effects of torsional restraint created in the upper stem or stem 2 of the pseudoknot during ribosome-induced unfolding of stem 1 in regulating −1 PRF efficiency have also been studied by different groups[29] and provide fresh insights into structural intricacies of pseudoknots and the complexity of the −1 PRF process.[30,31] Molecular dynamics studies carried out on Mouse Mammary Tumour Virus (MMTV)[32] and BWYV RNA pseudoknot[33] involved in −1 PRF illustrated novel dynamic aspects of the structure.

Despite recent progress in the availability of structural information for frameshift pseudoknots from crystallographic, chemical probing, and comparative sequence analysis data,[34] a precise mechanism underlying −1 PRF is still not completely understood. Several mutational studies on functional frameshift pseudoknots suggest that the overall global structure of the functional and nonfunctional forms is similar.[35] Though some mutations in the pseudoknot have been shown to enhance the frameshifting efficiency up to 2−3-fold with respect to their wild-type counterparts,[35,36] other mutations have reduced this efficiency. One such mutational study[36] systematically demonstrated the effect of mutating each residue of Beet Western Yellow Virus (BWYV) frameshift pseudoknot on the efficiency of −1 PRF. The rationale behind terming a pseudoknot functional or nonfunctional in these studies was based on whether a particular mutation increased/decreased the efficiency with which the structure can induce −1 PRF. These studies suggested that the efficiency of a −1 PRF-inducing pseudoknot is a function of minute structural

characteristics dispersed throughout the structure. Here we have tried to understand the structural ramifications of some of these mutations on the dynamic behavior of the BWYV RNA pseudoknot and identify the reasons behind gain or loss of efficiency in −1 PRF. A series of molecular dynamics simulations spanning a total time period of 1.55 μs have been carried out on this pseudoknot, using the 1.25 Å resolution crystal structure.[37] The crystal structure reports the presence of six magnesium ions, three sodium ions, and one potassium ion, along with a total of 180 water molecules, including those that form the first hydration shell of magnesium ions. For studying mutated structures, we selected four different mutations, out of which two were reported to cause an increase and the remaining two caused a decrease in efficiency of −1 PRF.[38] Each of these four mutations represented the following categories of functional outcomes, viz., a moderate increase/drastic increase in efficiency and a moderate decrease/drastic decrease in efficiency. These variants differ from the native state by base-pair inversion in stem 1, single base substitution in loop 2, base-pair inversion in stem 2, and isosteric base-pair replacement in stem 1. We have specifically addressed the following questions: why did G4C:C17G base-pair inversion and A25C substitution lead to an increase in −1 PRF efficiencies, why G7A:C14U and C11G:G27C base-pair replacements lead to a decrease in the efficiencies of the BWVY pseudoknot, the role of protonated C8 in maintaining structural integrity, and finally, testing the effect of the magnesium ions on the global conformation of this structure. These effects were assessed in terms of parameters like change in Watson−Crick/non-Watson−Crick hydrogen bonds, helical geometries, structural fluctuations, hydration, and water-mediated hydrogen bond patterns and ionic densities in wild-type and mutant BWYY pseudoknot structure. To analyze the amino acid environment around the pseudoknot at the mRNA
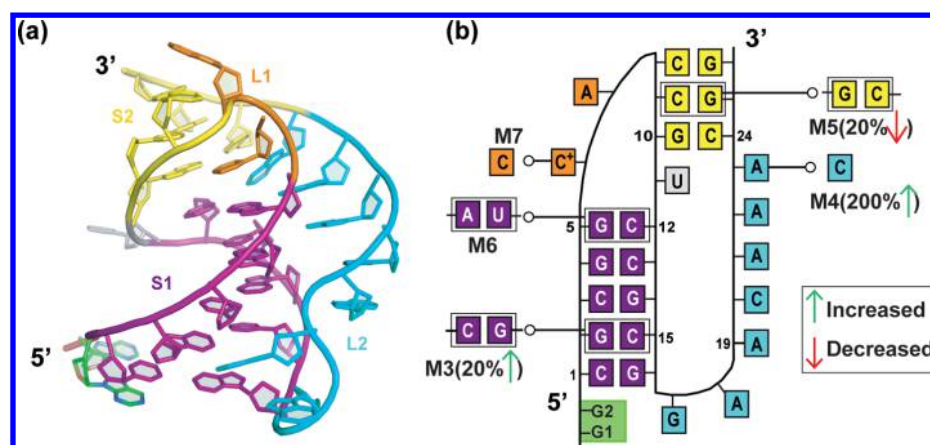
11906

dx.doi.org/10.1021/jp507154u | J. Phys. Chem. B 2014, 118, 11905−11920

Figure 2. BWYV RNA pseudoknot. (a) Tertiary structure of BWYV RNA pseudoknot (PDB file 1L2X); S1 indicates helix 1, S2 indicates helix 2, L1 and L2 are loops 1 and 2, respectively. (b) Schematic showing various mutations studied here and final renumbering of the residues after pruning the initial 2 guanine residues shown in the green box.

entry tunnel and potential protein−RNA contacts, the X-ray structure of eukaryotic 40S ribosomal subunit was fitted into the cryo-EM density map of the eukaryotic 80S ribosome.[28]

■ **METHODS**

Description of Starting Systems. The initial structure for the native state simulation was taken from the refined model of BWYV frameshift pseudoknot (PDB ID: 1L2X) solved at 1.25 Å resolution.[37] Due to the presence of many ions, ion-associated and independent water molecules, we cautiously kept only the biologically relevant residues in the starting geometry. Because the two terminal guanine residues G1 and G2 are not part of the wild-type sequence, they were omitted from the final structure considered for simulation and remaining residues were renumbered for clarity (Figure 2). We also removed one potassium ion K64 and two magnesium ions Mg29 and Mg59 (X-ray structure numbering) as it was reported that these residues were inconsequential for biological activity of the native structure.[37] The numbering used for magnesium ions in this work corresponds to that given in the crystal structure PDB file (1L2X). All the water molecules, except those that either were involved in inner-sphere coordination with the remaining magnesium ions or were at a distance of ≤2.5 Å from these ions, were also removed. This resulted in a final pseudoknot structure with twenty-six nucleotide residues, four magnesium, three sodium ions, and twenty-one water molecules forming first hydration shell of magnesium ions. This starting conformation represented the native state M1. The BWYV pseudoknot also contains a protonated cytosine C6 in loop 1. Appropriate parameters were derived for this residue as mentioned below, as per methodology given elsewhere.[33]

The two gain of function mutations with respect to native structure (M1) were named M3 and M4, and loss of function mutations were termed M5 and M6 (Table 1). These mutant structures were prepared *in silico* using the *mutate_bases* module of the 3DNA[39] program. This module introduces base mutations such that the base reference frame (position and orientation) is maintained and the mutated structure shares the same base-pair/step geometry as that of the native or reference structure. Further, this module does not disrupt backbone conformation. A detailed description of the corresponding *in vitro* −1 PRF efficiency values of these mutants can be found in

Table 1. Description of Different Starting Structures from Beet Western Yellow Virus (BWYV) RNA Pseudoknot Investigated in This Study

system	description	no. of ions[a]	time (ns)
M1[b]	native state, C6+	4 Mg^{2+}, 16 Na$^+$	200
M2	native state without Mg^{2+} ions	24 Na$^+$	200
M3	mutant 1: G2 to C2, C15 to G15	4 Mg^{2+}, 16 Na$^+$	200
M4	mutant 2: A23 to C23	4 Mg^{2+}, 16 Na$^+$	200
M5	mutant 3: C9 to G9, G25 to C25	4 Mg^{2+}, 16 Na$^+$	200
M6	mutant 4: G5 to A5, C12 to U12	4 Mg^{2+}, 16 Na$^+$	200
M7	standard C6, unprotonated state	4 Mg^{2+}, 17 Na$^+$	250[c]

[a]Total number of ions in the final system to be simulated. [b]Wild-type efficiency (M1−10.8%). [c]Simulation time extended to solve convergence issues.

refs 36, 38, and 40. To study the structural significance of protonated C6 residue, another simulation (M7) was carried out with the standard, unprotonated cytosine. To investigate the behavior of pseudoknot in the absence of magnesium ions, simulation M2 was set up. Replicate simulations for each of these systems were also performed for better conformational sampling and verification of any significant structural transition (Supplementary Table 1, Supporting Information). For cryo-EM map fitting, the map reported by Namy et al.[28] was taken. This map consists of the eukaryotic 80S ribosome bound to tRNA and eEF2 with an IBV (Infectious Bronchitis virus) RNA pseudoknot stalled at the mRNA entry tunnel (EMD-1197, resolution 16.2 Å). Because our aim was to analyze the distribution of amino acids at the mRNA entry tunnel of ribosome that could potentially form contacts with stalled RNA, we focused on fitting only the small 40S subunit crystal structure[41] solved at 3.93 Å resolution into this map. The BWYV pseudoknot was fitted into the density corresponding to the IBV pseudoknot because it was our structure of interest and, second, an atomic resolution crystal structure of IBV has not been available to date. Moreover, the basic architectures of IBV and BWYV pseudoknots comprise a similar H-type topology, with the major difference being the length of the loop 2 region (∼32 residues in IBV as opposed to 7 residues in BWYV).[42] The 5′ and 3′-ends of BWYV pseudoknot were oriented by utilizing the information about the path mRNA traverses along the neck and shoulder of the 40S subunit.[43] Fitting done in this way appropriately positions our pseudoknot

11907

dx.doi.org/10.1021/jp507154u | J. Phys. Chem. B 2014, 118, 11905−11920

at approximately +13 to +14 position with respect to P-site tRNA.

MD Simulation Protocol. All atom classical MD simulations were performed using the pmemd module of AMBER[44] suite of programs. Here, we have used the ff99bsc0χ_{OL3} force field for all our simulations. All missing hydrogen atoms were added using the LEaP module of AMBER. The solute was neutralized with Na$^+$ counterions (radius 1.868 Å and well depth 0.002 77 kcal/mol[45]) whereas Mg^{2+} ions were placed according to the crystal structure. We did not include crystal sodium ions in any of the initial structures, and all the sodium ions were randomly placed using the LEaP module during counterion neutralization stage. All the systems were immersed in a box containing TIP3P[46] water molecules with a 10 Å thick layer around the solute edges. For Mg^{2+} ions, we used the recently proposed updated Villa et al.[47] set of parameters. Partial atomic charges for N3-protonated cytosine were derived according to procedure described earlier.[48] Gaussian09[49] was used for geometry optimization using HF/6-31G* scheme. The optimized geometry was then used for partial charge derivation employing the standard RESP scheme[50] using the R.E.D.-III[51] program.

Initial minimization was performed for 3000 steps by keeping a large restraint of 300 kcal/(mol A^2) on RNA heavy atoms and ions followed by a second minimization of 3000 steps with a reduced restraint of 100 kcal/(mol A^2), applied only on RNA heavy atoms. A constant volume 40 ps long MD with restraints of 100 kcal/(mol A^2) on RNA heavy atoms was done for solvent relaxation. A full system minimization of 2000 steps with no restraints was carried out subsequently, followed by 10 ps long multiple MD runs during which the restraints were progressively reduced from 50 to 5 kcal/(mol A^2) on all the heavy atoms except water and ions. A final minimization of 1000 steps was carried out to ensure the removal of any steric clashes left. A stepwise heating was carried out from 0 to 50 K in 10 ps, 50−150 K in 20 ps and 150−300 K in 30 ps under NvT conditions. The system was then finally equilibrated in NpT conditions for 100 ps (298 K, 1 atm) with an integration time step of 2 fs. Production stages were further carried out using a particle-mesh Ewald (PME).[52,53] SHAKE algorithm was applied to constrain all bonds containing hydrogen atoms. This protocol has been established in our lab and elsewhere.[48,54,55] The final production run was carried out for 200 ns in simulations from M1 to M6. For M7, this time was extended til 300 ns due to C6 flipping, but analysis was done for 250 ns of data.

Analysis of Trajectories. All the trajectories were analyzed using the cpptraj module of AMBER, and structures were visualized using PyMOL and UCSF-Chimera.[56] NUPARM[57] was used for analysis of various helicoidal parameters and backbone torsion angle calculation. For calculating the average RMSD and hydrogen bond lengths, final 160 000 snapshots were considered in all trajectories. The distance cutoff for calculating WC hydrogen bonds was kept to be 3.5 Å and the angle cutoff was 135° and for NWC hydrogen bonds this cutoff was increased to 4.0 Å. Only those hydrogen bonds having an occupancy >50% were considered significant for analysis. The Leontis−Westhof base-pair classification scheme is used to represent base-pair geometries.[58] Hydration analysis was performed by contouring water density on a grid of 0.5 Å^3 and contours were mapped onto minimized average structures from last 80 000 frames collected at 2 ps interval. Analysis of water-mediated interactions was done by careful visualization of

the trajectories and monitoring the positions of closest waters to the RNA solute. Hydration numbers were calculated by counting only those waters that were at a distance of ≤3.5 Å from RNA heavy atoms. Only those sites having >50% water occupancies were analyzed. Analysis of water-mediated hydrogen bonds found in the crystal structure was done by using HBPLUS.[59] Calculation of electrostatic potential maps was done using APBS software,[60] and resulting potentials were mapped onto the solvent accessible surface areas of last 10 ns average structures. For stacking area calculation, we chose snapshots at 2 ps intervals equally spaced throughout the trajectory, and stacking overlap calculations were done using 3DNA[39] software. UCSF-Chimera was used for fitting of crystal structures into the cryo-EM maps. The fitting procedure was iteratively performed so as to maximize the correlation between the EM data density and electron density obtained from the atomic structures (average optimized correlation −0.7). This method has been followed in previous studies.[61]

■ RESULTS AND DISCUSSION

Geometry of the Native Structure. This structure comprises two helical stems (S1 and S2) separated by two loops (L1 and L2). Stems S1 and S2 consist of five and three Watson−Crick base pairs, respectively, whereas L1 consists of two residues and L2 has seven unpaired residues (Figure 2). The BWYV pseudoknot structure has been studied extensively for the presence of various noncanonical base pairs between stem-loop residues as well as water-mediated interactions.[37,62] The crystal structure reveals that apart from the four GC and four CG Watson−Crick (WC) pairs in the helical stem region, there are a total of six non-WC (NWC) pairs between S1-L2 and S2-L1 mediated by direct base−base contacts. A description of NWC pairs and their nomenclature is shown in Supplementary Figure S1 (Supporting Information). The crystal structure has 180 water molecules out of which only a few are involved in formation of water-mediated hydrogen bonds with nucleic acid residues, whereas some others are involved in formation of inner-sphere contacts with Mg^{2+} and Na$^+$ ions.

Pseudoknot Dynamics in Simulation M7 Indicate Importance of Protonated Cytosine in Loop L1 in Maintaining Junction Geometry. The root-mean-square deviations of different structures with respect to their starting geometries provide a preliminary account of structural modulations as a result of change in the native conformation. For this purpose, separate RMSDs were calculated for all heavy atoms in the structure, as well as for backbone, helix, and loop heavy atoms (Supplementary Table 2, Supporting Information). In all the simulations, including replicate sets, the trajectories achieved a stable state after initial 20−30 ns. The largest deviations were observed to occur in certain loop regions (Supplementary Figures S2−4, Supporting Information). Overall, the deviations seen in stems S1, S2 and loop heavy atoms at different periods of time during some particular MD simulations clearly indicated that the specific changes and mutations made in the systems affect local geometries rather than the overall global conformation. For example, in simulation M7, the RMSD of loop heavy atoms increased slightly at 150 ns and at 180 ns; there was a sudden jump in the average RMSD value from 2.1 to 3.7 Å for loops L1 and L2. We observed that, until 150 ns, the conformation of N3-unprotonated cytosine C6 retained its initial state resembling crystal structure geometry where it was forming a Hoog-
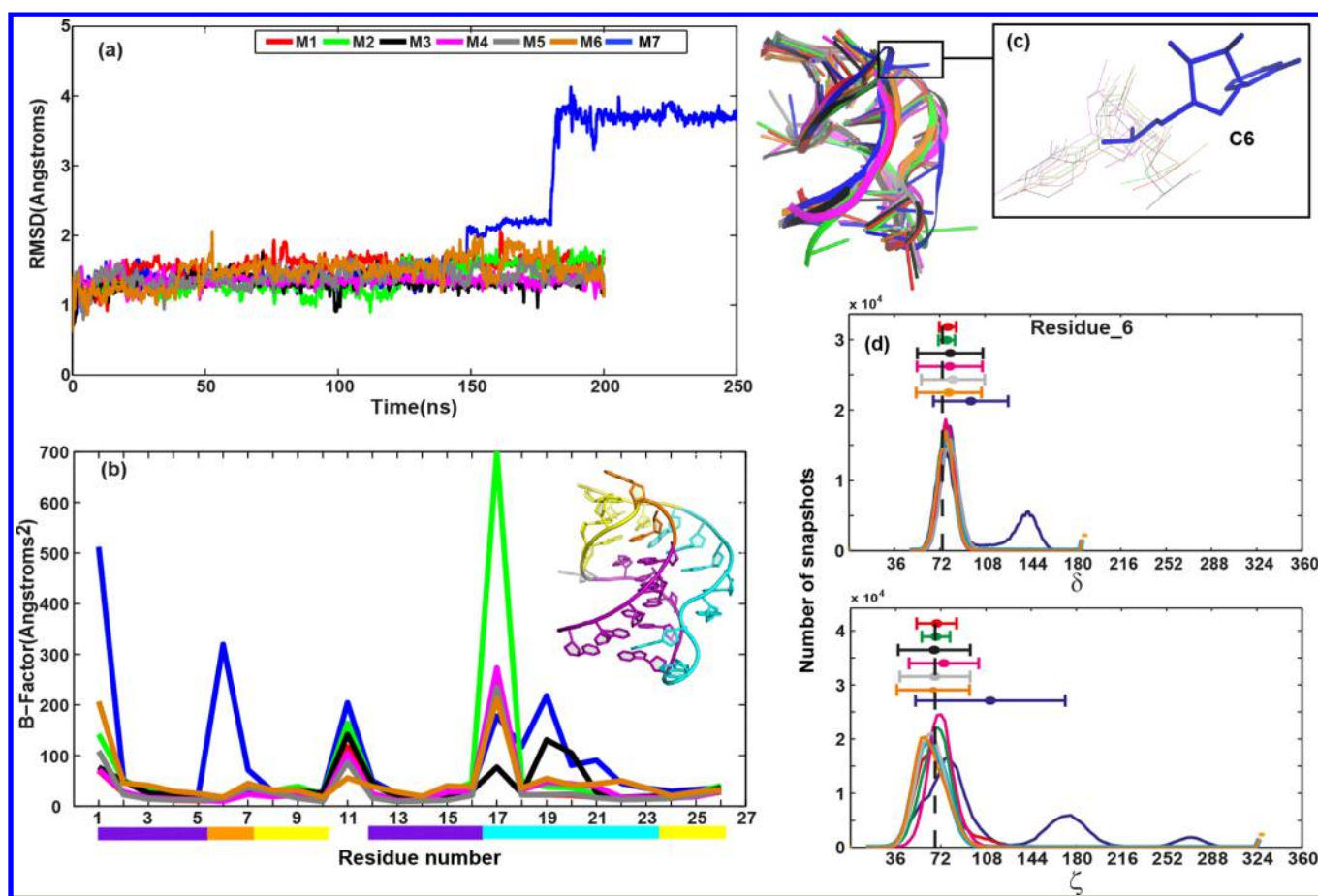
Figure 3. (a) RMSD for non-hydrogen atoms of the junctional "core" comprising residues G5, C6, G10, C12, A23, and C24. (b) RMS fluctuation in terms of B-factors for each residue with respect to the starting geometries. (c) Superposition of the backbone of the structures from the last snapshots taken from all the trajectories. Flipping of C6 in simulation M7 is shown in the box. The color coding indicates that of the corresponding simulation set. (d) Corresponding backbone torsion angle changes in the C6 residue.

steen:Watson (+)T pair with residue G10, giving rise to a "platform" of C6:G10:C24 bases (Figure 3, Supplementary Figure S5, Supporting Information). After 150 ns, N3-unprotonated C6 underwent a transition in the backbone torsion angle δ (about the C4′−C3′ bond) from 75° to 140°, along with a change in χ (about the C1′−N1/N9 bond) from an average value of 195° to 250° and in ζ (about the O3′−P bond) from 72° to 172°, which rendered it in an alternative conformation where it moved away from this platform for the rest of the trajectory. This motion was also observed in one of two replicate sets of M7. The conformational change of C6 was coupled with a larger disorder observed among L2 residues as well. This transition indicated the importance of protonation at N3 position of C6 to the maintenance of junction geometry as this flipping motion disrupted the neighboring NWC bonds between S1 and L2 and the stacking pattern L2 residues (Supplementary movie M1, Supporting Information). Apart from loop regions, short but reversible transitions were observed in stem S1 in simulations M6 and M7 (Supplementary Figure S2C, Supporting Information), caused mainly due to the terminal C1G16 base-pair fraying observed in these two cases. A transient, partial disruption of two S1 base pairs G2C15 and C3G14 was observed between 80 and 160 ns in M6, which coincided with a rearrangement of residues in L2 (Supplementary movie M2, Supporting Information). To further assess the effect of mutations on the stable pseudoknot

junction core comprising residues G5, C6, G10, C12, A23, and C24, we analyzed their RMSDs separately with respect to their starting geometries (Figure 3a). Except in the case of M7, where C6 was flipped out, the aforementioned core region retained its initial geometry suggesting that the N3-protonated C6 strongly held the pseudoknot junction together and stabilized it. Hence, any structural distortion in this region is highly inhibitory for the optimal functioning of the pseudoknot.

To dissect the residue-wise contribution toward structural fluctuations, we calculated the thermal B-factors for all the residues in various sets (Figure 3b). In all the cases investigated, residues U11 (at the junction between S1 and S2) and G17 (first residue of L2) displayed the highest B-factors, consistent with the fact that these two residues remain in an unpaired state and are not involved in hydrogen bond formation at any point of time with other residues. However, some exceptions to the above generalities were observed. In M6, a low B-factor value was observed for residue U11, due to a transient base-pair formation between U11 and A5. Similarly, smaller fluctuations were observed for residue G17 in simulation M3, whereas they were higher in M2 as a result of a change in the neighboring ionic environment. Overall, in the two mutations introduced near the pseudoknot junction viz. M7 and M6, the fluctuations in L2 residues A21, A22, and A23 were high, due to loss of crucial cWS and tWS type of hydrogen bonds formed by these
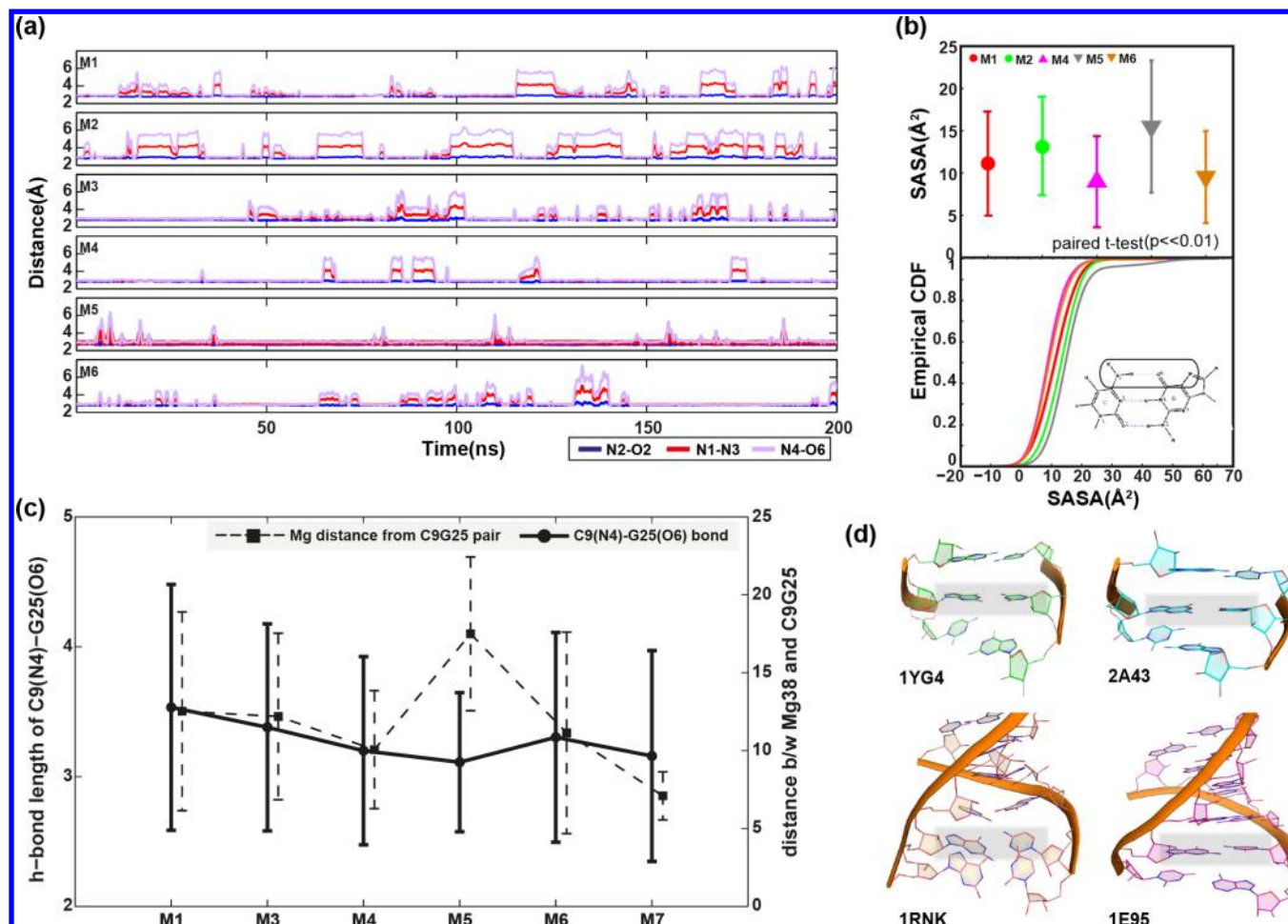
11909

dx.doi.org/10.1021/jp507154u | J. Phys. Chem. B 2014, 118, 11905−11920

Figure 4. (a) Behavior of the hydrogen bonds of C9G25 pair (stem S2) in different simulations. The lower limit of all the y-axes starts from 2 Å. (b) Mean SASA values of C9G25 pair (G9C25 in M5). Major groove atoms of the C9G25 pair were considered for calculating SASA values. (c) Correlation between the mean C9(N4)−G25(O6) distance and Mg38 separation from this pair. (d) Stem 2/upper stems from frameshift stimulating pseudoknots taken from different animal and plant RNA viruses. CG pairs are indicated in gray boxes.

residues with G4C13 and G5C12 pair in the native structure (M1).

The extremely sturdy and rigid global conformation maintained by BWYV pseudoknot in almost all the simulations indicated that ribosomal recognition and subsequent pausing to cause optimal frameshift efficiency is modulated by a number of localized discrete factors that are distributed throughout the pseudoknot. Therefore, a rise or fall in efficiency due to various mutations could be best explained by recognizing the local conformational changes in the pseudoknot rather than attributing them to some global alterations in the structure.

Putative Direct Contact between Ribosome and Pseudoknot Base Pair: Indications from Recurrent Opening of the C9G25 Pair. The WC base pairs in stems S1 and S2 were found to be stable in terms of number of base pairs observed during the simulation and individual hydrogen bonds in each pair (Supplementary Tables 3 and 4, Supporting Information). Terminal base-pair C1G16 in S1 was less stable compared to the terminal C8G26 pair in S2, due to the fact that residue A7 of L1 partially stacks on top of C8 ring, hence minimizing the terminal base-pair fraying effects and increasing the effective length of helix S2 (Supplementary Figure S6, Supporting Information). However, base-pair C9G25 displayed an intermittent partial opening in M1 (Figure 4a), during which a water molecule interrupted the direct atomic contacts

between C9(N4)−G25(O6) atoms (Supplementary Figure S10c, Supporting Information). This partial opening was marked by negative base-pair shear of residue C9. This behavior was found to be transient and reversible and the extent of its occurrence varied between 10 to 30 ns time spans in sets M1, M2, M3, M4, and M6. But, in loss of function mutant simulation M5, where we inverted the C9G25 pair with G9C25 pair, this trend was rarely observed and lasted only for a few picoseconds. All three hydrogen bonds of the G9C25 pair were stable in M5 (Figure 4a). However, in simulation M2, which was carried out in the absence of magnesium ions, the occurrence of this partial opening was highest with longer residence times. The implications of these observations could be manifold. First, in the crystal structure,[37] the role of Mg38 was not clear, but it was shown that it formed water-mediated contacts with N7 and O6 of neighboring G25 and G26 residues. We observed that this magnesium ion maintained its aforementioned contacts in stem S2 throughout the native structure simulation (M1). By contrast, M2, which is devoid of any crystal structure, determined magnesium ions showed recurrent partial opening of this pair. It was observed that in M2 simulation, up to two Na⁺ ions simultaneously occupied this position, which was taken in other cases by Mg²⁺ ion. This event indicated that Mg38 was not only involved in maintaining water-mediated contacts with successive guanine residues in
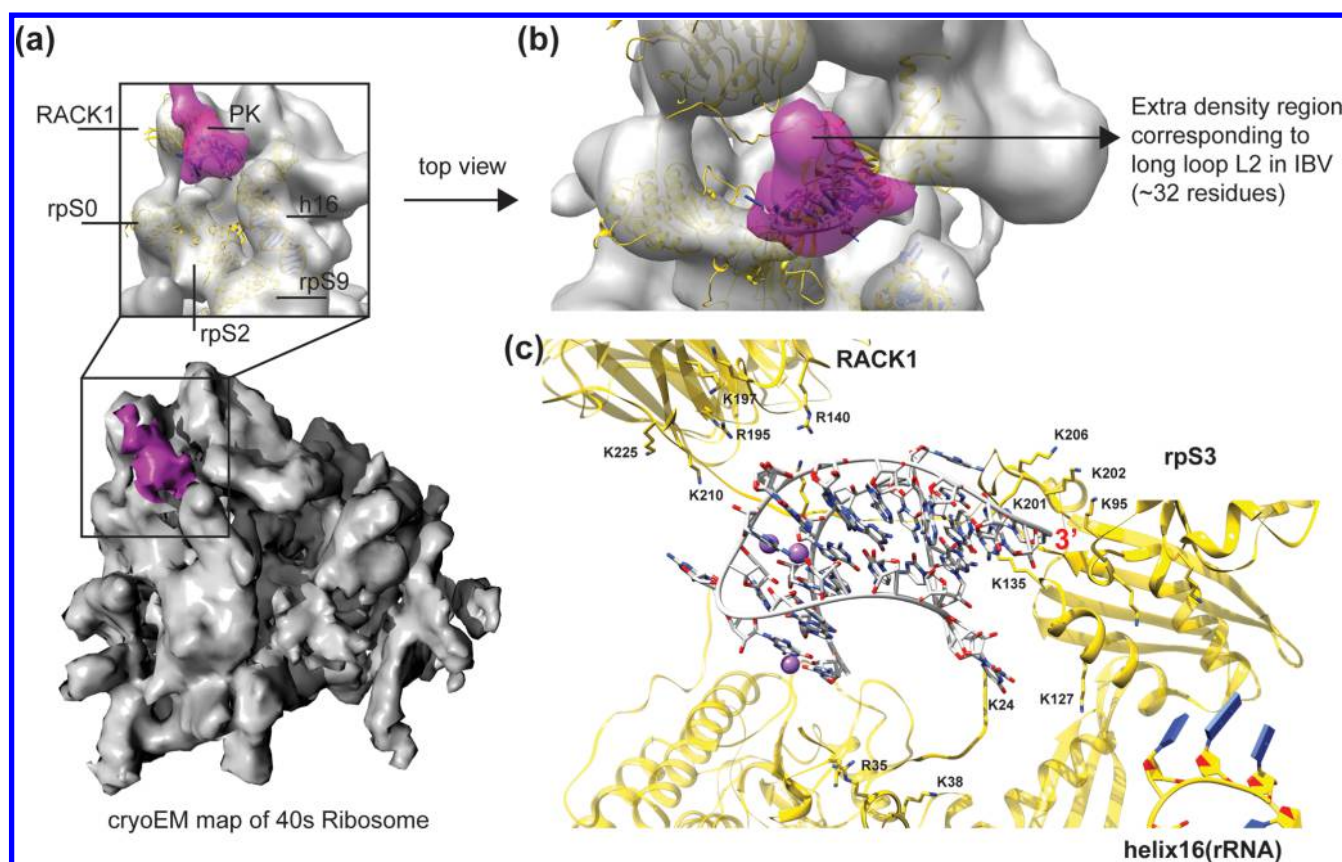
Figure 5. (a) Cryo-EM map of eukaryotic ribosome with IBV pseudoknot (magenta) and tRNA. The inset shows an enlarged view of the mRNA entry site blocked by the incoming pseudoknot and surrounded by 40s ribosomal proteins RACK1, rpS3, helix16 (18srRNA), rpS9, rpS2, and rpS0. (b) Top view showing the most probable orientation of BWYV fitted in the IBV pseudoknot density map. (c) The mRNA entry region is surrounded by several positively charged amino acid residues.

stem S2 but also maintained the optimum geometry of base pairs in this region. Second, the inversion of C9G25 by G9C25 in M5 led to a loss of consecutive O6 and N7 groups in G25 and G26, disturbing the water-mediated contacts and magnesium binding discussed above and resulting in a stable G9C25 pair with a reduced open angle.

To verify these claims, the solvent accessible surface area (SASA) was calculated for major groove facing atoms of the C9G25 base pair (Figure 4b, upper panel). The contribution of C9(N4), G25(N7, O6) groups toward total solvent accessible surfaces varied significantly among various simulated structures, which was further confirmed by the overall distribution of these values during the corresponding trajectories (Figure 4b, lower panel). Especially, simulation M5 displayed the greatest deviation for the SASA distribution in the cumulative distribution curve (CDF), indicating that C9G25 inversion to G9C25 was indeed detrimental for the pseudoknot frameshift efficiency as it might influence the correct base-pair geometry required for ribosome recognition. Furthermore, when the mean distance between Mg38 from the center of mass of the C9G25 pair was compared against the mean hydrogen bond distance between C9(N4)–G25(O6) in different trajectories (Figure 4c), the trend displayed by M5 was in perfect accordance with the observations made above. The C9G25 base-pair inversion was causing Mg38 to drift away from this site and affect the resulting pair geometry. All the optimum functioning (M1) and gain of function mutants (M3, M4) displayed a tendency toward large negative propeller twist positive open angle for S2 pairs, resembling crystal structure

values. In mutant M5, the range of base-pair parameter values in stem S1 was comparable to the native set, but significant deviations were observed for buckle and propeller twist values in S2 pairs C8G26 and G9C25 (Supplementary Figure S14, Supporting Information). The geometry of C9G25 and neighboring base pairs in S2 plays an important role in optimum functioning of the pseudoknot, which is further verified by the fact that similar CG base pairs in stem S2 of other pseudoknots also prefer a high propeller twist and open angle values (Figure 4d[40,63−65]).

This theory was further tested by fitting the atomic structure of 40s ribosomal subunit (PDB 2XZM)[41] into the cryo-EM map of the 80s ribosomal subunit.[28] We looked for amino acid distribution around the BWYV pseudoknot in the ribosomal proteins RACK1, rpS3, and rpS2 present at the mRNA entry site. Because these proteins also form contacts with 18s rRNA, we focused our analysis on the solvent exposed surface of these proteins where they do not form any contacts with rRNA. In this region, multiple lysine and arginine residues were found that projected their side chains into the groove, which corresponded to the space occupied by pseudoknot density (Figure 5). A closer look at this interface region revealed that Lys95, 201, 202, 206, and Lys135 in rpS3 could potentially interact with the pseudoknot during the unwinding process and lay in close proximity to stem S2. In protein RACK1, Arg140, 195 and Lys197, 210, and 225 residues could also interact with loop L2 of the BWYV pseudoknot. Interestingly, after fitting BWYV structure, an additional density region near L2 was observed that lay in close proximity to the protein RACK1. The

Table 2. Average Hydrogen Bond Lengths of NWC Interactions and Their Percent Occurrence Values[a]

pair[b]	M1 (wt) mean[c]	%	M2 mean	%	M3 mean	%	M4 mean	%	M5 mean	%	M6 mean	%	M7 mean	%	X-ray
G2(N2)_A18(N3)[d]	2.9 (0.1)	100	3.0 (0.1)	100			3.0 (0.1)	100	3.0 (0.1)	100	3.0 (0.1)	100	3.8 (0.9)	47	3.0
G2(O2′)_A18(N1)[d]	2.9 (0.2)	85	2.9 (0.2)	86	3.1 (0.3)	68	2.9 (0.2)	75	2.9 (0.2)	83	2.9 (0.2)	89			2.7
C15(O2′)_A18(O2′)[d]	3.4 (1.1)	77	4.0 (1.5)	66	3.0 (0.6)	83	2.9 (0.6)	93	3.1 (1.0)	88	3.3 (0.6)	53			2.7
G4(N2)_A21(N1)													3.7 (1.4)	63	5.5
C13(O2′)_A21(N1)	2.9 (0.3)	84	2.9 (0.2)	86	2.8 (0.2)	87	3.3 (0.8)	60	2.9 (0.3)	85					2.7
C13(O2)_A21(N6)	3.2 (0.4)	87	3.2 (0.3)	89	3.2 (0.3)	87	3.9 (1.0)	64	3.2 (0.4)	86					3.1
G5(N2)_A22(N1)[e]	3.1 (0.2)	100	3.1 (0.1)	100	3.1 (0.2)	100	3.0 (0.1)	100	3.2 (0.4)	95			3.6 (1.2)	72	3.0
G5(N2)_A22(N6)[e]	3.5 (0.2)	36	3.5 (0.2)	42	3.6 (0.2)	54	3.6 (0.2)	57	3.6 (0.2)	47					3.7
G5(N3)_A22(N6)[e]	2.9 (0.1)	94	2.9 (0.1)	95	2.9 (0.1)	95	2.9 (0.1)	96	3.0 (0.2)	90			3.3 (0.9)	69	2.9
G5(O2′)_A22(N6)[e]	3.0 (0.2)	81	3.0 (0.2)	76	3.0 (0.2)	78	3.0 (0.2)	72	3.1 (0.5)	77			3.4 (1.2)	57	3.0
C12(O2′)_A23(N1)[fg]	2.9 (0.5)	92	2.8 (0.2)	92	2.9 (0.3)	89	2.9 (0.2)	80	2.8 (0.1)	97	3.4 (0.9)	70	2.8 (0.1)	86	2.7
C12(O2)_A23(N6)[fg]	3.1 (0.4)	88	3.1 (0.3)	82	3.0 (0.2)	88	3.0 (0.3)	66	3.0 (0.2)	92	3.5 (1.0)	64	3.0 (0.2)	85	2.8
C6(N3)_G10(O6)	2.8 (0.1)	98	2.8 (0.1)	98	2.8 (0.1)	99	2.8 (0.1)	96	2.8 (0.1)	98	2.9 (0.1)	97			2.7
C6(N4)_G10(N7)	2.9 (0.1)	95	2.9 (0.1)	95	2.9 (0.1)	96	2.9 (0.1)	94	2.9 (0.1)	92	2.9 (0.1)	98			3.0
C6(O2)_A23(N6)[h]	3.3 (0.7)	87	3.2 (0.4)	88	3.4 (0.5)	84	3.0 (0.2)	99	3.7 (0.8)	68					2.9
G14(N2)_A19(OP2)	3.5 (0.9)	64	3.31 (0.8)	74			3.5 (0.9)	58	3.2 (0.7)	82					2.9
G14(O2′)_A19(N6)	3.3 (0.7)	74	3.6 (1.03)	60					3.3 (0.6)	65					3.1
A7(O2′)_C8(OP1)			3.3 (0.9)	67			2.9 (0.5)	89	3.3 (0.9)	62					4.8
A7(OP1)_C8(N4)			3.6 (0.9)	72			3.2 (0.6)	86	3.9 (1.2)	54					2.9
C3(O2)_A18(O2′)	3.2 (0.5)	51	3.4 (0.6)	43	3.2 (0.4)	53			3.2 (0.5)	59					2.9
G17(N2)_G17(OP2)					3.9 (2.3)	68									9.4
G17(O2′)_A18(OP1)					2.7 (0.2)	91	3.6 (1.0)	46	3.2 (0.8)	56					4.7
A22(O2′)_A23(O5′)[i]	3.1 (0.2)	74	3.1 (0.2)	79	3.1 (0.2)	74	3.1 (0.2)	65	3.1 (0.2)	73			3.2 (0.3)	52	4.2

[a]The values from MD simulated and X-ray structures are listed. All distances are in Å. [b]Pair indicates the hydrogen bond donor−acceptor group. [c]Mean values calculated from equilibrated trajectories (initial 40 ns not considered for averaging). Standard deviation values are listed in parentheses. [d]Hydrogen bond values correspond to donor−acceptor location as that of M1 for the C2G15 pair (C2{O2, O2′}, G15{O2′}) in M3. [e,f]H bond values corresponding to the A5U12 pair (A5{C2, N3, O2′}, U12{O2′, O2}), respectively, in M6. [g]H bond values corresponding to the C23 residue (C23 {N3, N4}) in M4. [h]C23(N4) in M4. [i]C23(O5′) in M4.

sequence of the IBV pseudoknot consists of a long loop L2 of ∼32 nucleotides, which could account for the presence of this density.[66] It further indicated the presence of additional contacts between RNA and ribosome. This evidence strongly suggests a specific position and geometry dependent recognition of nucleobase groups in the pseudoknot by ribosome and establishes a clear correspondence between specific base-pair geometry and functioning of the −1 PRF inducing pseudoknots.

Changes in the Pattern of Noncanonical Interactions between Stems and Loops Alter the Local Conformation and Stability in Mutants M6 and M7. An unambiguous effect of various mutations was seen at the level of NWC pairs found in the pseudoknot structure. To visually
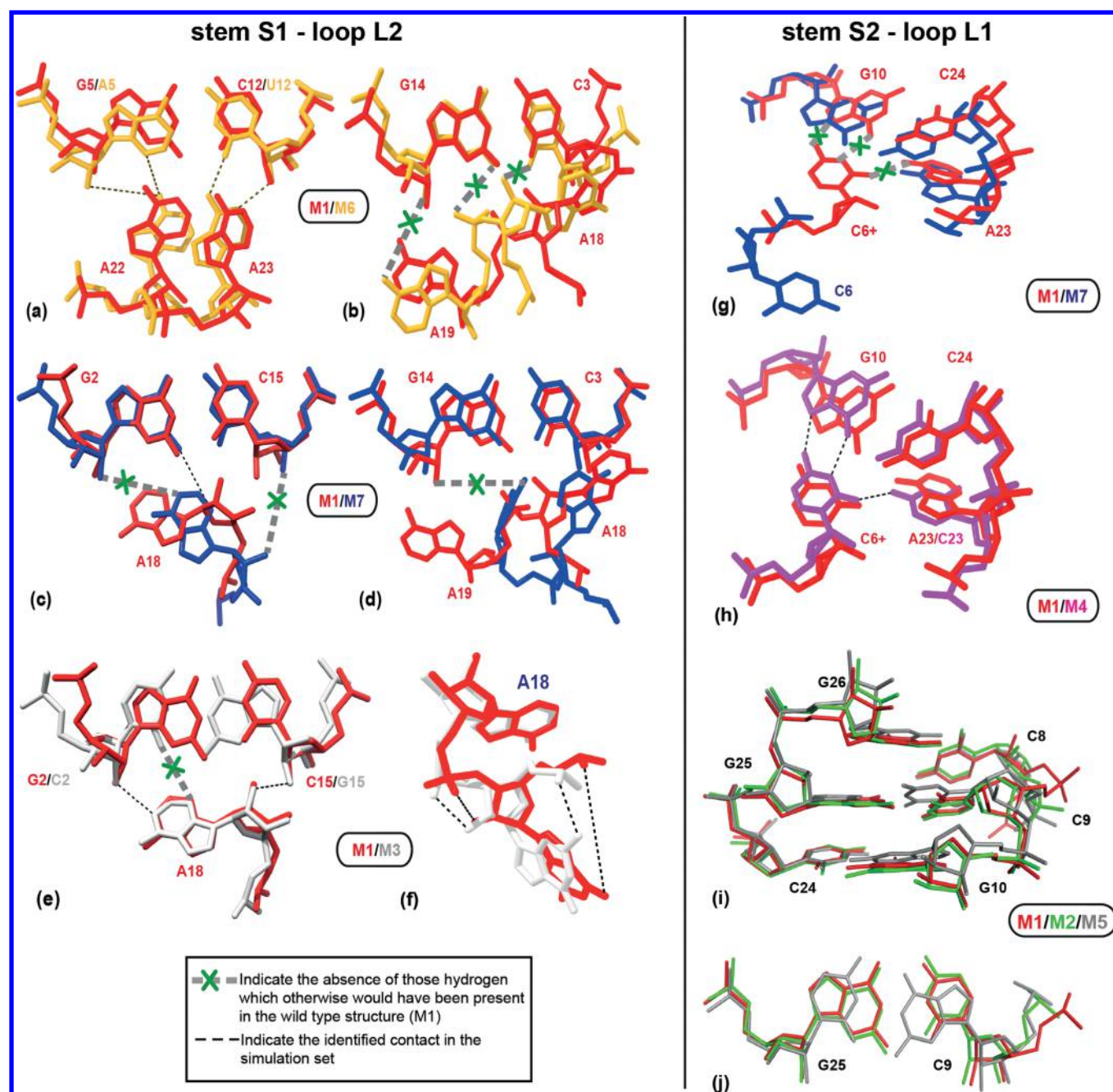
Figure 6. Schematic representation of major NWC interactions. The color scheme adopted for various mutants resembles that adopted for plots in Figure 2. (a, b) M6 on M1 showing the absence of noncanonical hydrogen bonds between G5(A5):A22/C12(U12):A23 and G14:A19/C3:A18. (c, d, g) M7 on M1 showing noncanonical hydrogen bonds between G2:A18, C15:A18, G14:A19, and C6:G10:A23. (e, f) M3 on M1 showing hydrogen bonds between G2(C2):A18 and G17:A18. (h) M4 on M1 showing hydrogen bonds between C6:G10:A23. (i, j) Backbone superposition of stem S2 in M1, M2, and M5 simulations and C9G25 pair.

analyze any relative change in the spatial placement of residues in the mutant structures, a superposition of the average structures from the last 10 ns of all simulations with respect to the backbone of their corresponding initial structures was done. At the interface of stems S1 and S2, residues C12 and A23 form a cSW hydrogen bond. Hydrogen bonds at positions corresponding to C12(O2′)−A23(N1) and C12(O2)−A23(N6) atoms were found to be stable in all systems, with high occurrence values in M4 (A23C) and low in M6 (G5A-C12U) (Table 2). The presence of A5U12 in place of the G5C12 base pair in M6 did not affect the formation of hydrogen bonds involving the U12 residue. Consequently,

U12(O2′)−A23(N1) and U12(O2)−A23(N6) bonds were retained in M6, albeit with slightly lower occurrences, relative to other sets. On the other hand, this substitution had a profound effect on cSW pairing normally occurring between G5(N2)−A22(N1), G5(N3)−A22(N6), and G5(O2′)−A23(N6). When the G5 residue is replaced with an A5 in M6, the resulting absence of the 2-amino group in the A5 residue at the sugar edge renders it incapable of participating in any kind of NWC contact with loop residue A23 (Figure 6a). We observed that the distance between the remaining two hydrogen bonding sites in A5 viz. A5(N3)−A22(N6) and A5(O2′)−A22(N6) was much beyond the limits of the

11913

dx.doi.org/10.1021/jp507154u | J. Phys. Chem. B 2014, 118, 11905−11920

distance required for stable hydrogen bond formation. The occurrence of NWC hydrogen bonds formed between G5:A22 residues was found to be low in the M7 set too, compared to the native structure simulation, especially due to increased fluctuation of L2 residues (Table 2). As an additional measure for comparing the hydrogen bond changes, we calculated various intra base-pair parameters for S1 and S2 (Supplementary Figure S14, Supporting Information). For the G5C12 pair, the M4 mutant displayed a relatively large negative propeller twist and negative shear values with respect to simulation M1 and other mutant sets. A negative shear suggested the slight displacement of C12 into the minor groove of S1 to form stable NWC hydrogen bonds with C23. In the M6 set, a highly reduced propeller twist angle and positive shear was observed for A5U12 pair, which corresponded well with the loss of A5:A22 tSW interaction. The trends in base-pair parameters buckle, propeller twist, open angle, shear, and stretch varied significantly for other base pairs of M6 mutant structure as well. Apart from adversely affecting the hydrogen bonds formed at the pseudoknot junction, the two mutations at or near this region, i.e., M6 and M7 (C6+ to C6), were found to further distort the geometry of the neighboring cSW pairing between C13:A21 and G14:A19. Again, an altered conformation arising due to an increased fluctuation in L2 residues in both M6 and M7 affected the hydrogen bonds between G2(O2′)−A18(N1) and C15(O2′)−A18(O2′) (Figure 6b−d). This observation keenly coincided with a large positive open angle observed for base pairs G2C15 and C3G14 in M6, during a time scale ranging from 50 to 100 ns. It indicated a base pair opening in the major groove, during which the WC hydrogen bonding between these two pairs was partially disrupted (Supplementary movie M2, Supporting Information). This event was almost immediately succeeded by a rearrangement of L2 residues characterized by a change in their base stacking arrangement, which was followed by progressive loss of NWC hydrogen bonds in this region in M6 and M7 (Supplementary Figure S7, Supporting Information). In M3 (G2C15 to C2G15) and M4 (A23C), where a gain in efficiency was reported, formation of some new noncanonical hydrogen bonds in other regions of the pseudoknot was observed. These additional hydrogen bonds might assist in stabilizing the geometry either at the base of the structure at the 5′ end or at the junction. To verify this, a careful analysis of these additional hydrogen bonds and their relevance in the context of efficiency of the BWYV pseudoknot was performed.

Additional Hydrogen Bonds in Mutants M3 and M4 Increase Local and Global Stability of the Pseudoknot, Respectively. The occurrence of two additional potential hydrogen bonds after 15 ns of simulation was quite striking in our simulations, first, between A22(O2′)−A23(O5′) and, second, between A7(O2′)−C8(O1P) (Supplementary Figure S8a,b (Supporting Information); Table 2). These hydrogen bonds were found to be more stable in gain of function mutants (M3 and M4) and showed less standard deviation compared to the loss of function mutations M6 and M7, which displayed higher mean values. It was observed that A23C substitution in M4 increased the stacking area overlap between A7 and C8, as the average stacking area between these two residues was 4.3 Å (±1.2 Å) in M4 against an average value of 3.8 Å (±1.3 Å) in the M1 set (Supplementary Figure S6, Supporting Information). This improved stacking in turn gave rise to strong hydrogen bonds between the phosphate backbone of A7 and

C8 residues. The latter bond between A7(O2′)−C8(O1P) was a revelation of M4 set, being considerably stable in terms of mean length relative to the native (M1) set, evident from high occupancy values. In M3, the N2 and O1P groups of residue G17 came close enough to give rise to an intra-residue hydrogen bonding contact that was absent in other cases. The mean distance between these two groups was 3.9 Å; way below what was observed in wild-type structure (10 Å) (Figure 6f, Table 2). Furthermore, this mutant also showed a reduced separation of ∼2.7 Å between G17(O2′) and A18(O1P), suggesting the presence of a hydrogen bond between these consecutive loop residues (Table 2). It can be speculated that the presence of these extra bonds at the 5′ end of the pseudoknot might contribute toward enhancing the stability at the base of the structure that could delay the ribosomal pause and subsequent unfolding of the structure, thus leading to a moderate increase in efficiency.

A 2-Fold Increase in −1 PRF Efficiency by Mutant M4 Arising from a Highly Stable Junctional Core Region. The only and, arguably, the most important base triplet in BWYV structure is formed by a Hoogsteen:Watson (+)T pairing between N3-protonated cytosine C6 and G10. The two C6(N3)−G10(O6) and C6(N4)−G10(N7) hydrogen bonds were the most stable NWC bonds in the native (M1) and mutant state simulation, except M7 where C6 was kept in normal unprotonated state (Table 2, Figure 6g). Apparently, this C6 also forms a hydrogen bond with L2 residue A23. Although a direct atomic contact between these two residues was not evident in native structure simulations, we did observe a direct hydrogen bond between C6(O2) and C23(N4) in mutant M4 (Table 2, Figure 6h). Cornish et al.[40] reported that the solution structure of wild-type Sugarcane yellow leaf virus (ScYLV) contains a naturally occurring cytosine C27 against A23 in BWYV. Incidentally, the *in vitro* wild-type efficiency of the ScYLV frameshift pseudoknot (15 ± 2%) is higher than that of BWYV (6 ± 1%). A backbone superposition of ScYLV and BWYV mutant M4 (A23C) junction residues (Supplementary Figure S9, Supporting Information) yielded an RMSD value of 0.9 Å and supported the fact that in the A23C mutant BWYV structure, C6+ can undergo a displacement to move closer to the G10−C24 base pair and form a direct contact with the C23(N4) atom. This movement of C6+ could also be facilitated by the absence of an imidazole ring in C23, which, otherwise, would sterically constrain this motion of C6+ (Figure 6h, Supplementary Figure S9a, Supporting Information). It further improved the stacking patterns between residues located at junction regions as inferred by dynamic cross correlation map analysis (DCCM) (Supplementary Figure S9b, Supporting Information). A comparison of DCCM maps between M1 and M4 yielded increased correlation between C6+ and C23, besides increasing the positive correlation between stem 1 pair G5:C12 and residues G5, C6+. Hence, A23C substitution stabilized the pseudoknot "junctional core" significantly apart from giving rise to additional hydrogen bonds between A7 and C8, leading to a highly compact pseudoknot that could resist ribosome-induced unfolding more effectively and increase the PRF efficiency. The effect of a structure that poses an increased resistance to unfolding is experienced at the codon:anticodon base-pairing between mRNA and tRNA at P- and A-sites in ribosome. As discussed in previous section, the increased strain at the mRNA entry tunnel, caused during the unwinding of a more robust pseudoknot by ribosome, will increase the strain at P- and A-

11914

dx.doi.org/10.1021/jp507154u | J. Phys. Chem. B 2014, 118, 11905−11920

site tRNAs,[28] which are involved in base-pairing with mRNA codons. This increased strain will facilitate the slippage of tRNAs on the slip-site, thereby increasing the efficiency of −1 PRF.

Modulation of Water-Mediated Hydrogen Bonds and Hydration Patterns by Mutations. The BWYV pseudoknot X-ray structure contained several water molecules out of which about 56 waters were found to interact directly with the pseudoknot via hydrogen bond formation mainly through the phosphate backbone. It was interesting to see that out of all the *in silico* mutations introduced, some clearly affected the overall hydration patterns of the native structure (Figure 7A). We analyzed major hydration sites in BWYV wild-type pseudoknot structure during the simulation and compared the location of these sites with that of critical crystal waters involved in the formation of hydrogen bonds with the structure. Changes observed in the mutant structures were analyzed with respect to reference state (M1). In M1, the junction interface of stems S1 and S2 was found to be highly hydrated but most of these sites were the result of waters coordinated to magnesium Mg45. Apart from bridging O6 and N7 atoms of adjacent G4 and G5 residues, the coordinated waters at the S1/S2 interface also form hydrogen bonds to the O1P of U11 residue, which faces the major groove of S1 (Figure 7A). Other sites of hydration, which included some of the free waters, were the O2P/O2′ groups of consecutive C12, C13, G14 residues in S1 and O1P/O2P/N6/N7 groups of A21, A22, A23 residues in L2 having maximum occupancies in this structure (Supplementary Table 5, Supporting Information). The observed positional occupancies of these sites critically corresponded to the location of waters in the BWYV crystal structure. Another high density water patch around the N3/O2 group of C6, N4 of C24 and N7 of A23 corresponded to a single water molecule that has the potential to form multiple hydrogen bonds in this region, as a number of hydrogen bond donor and acceptor groups are seated at this location (Supplementary Figure S10c, Supporting Information). Apparently, these sites were not observed in an earlier study,[33] presumably because of short time durations of the simulations. In addition to these regions, we also observed hydration sites that roughly corresponded to the crystal structure waters mediating hydrogen bonds between A7-(O2P)/C9(N4) and C6(N4)/C9(O2P) groups (Supplementary Figure S10c, Supporting Information). In the case where we removed magnesium ions from the initial geometry (M2) the resulting overall hydration patterns at 10 times bulk water density looked strikingly similar to the one reported by Csaszar et al.[33] (Supplementary Figure S11, middle panel, Supporting Information). Many sites found at the stem S1−S2 junction interface in the wild-type structure were missing in this case, most notable being the sites bridging G5 and G10 residues.

Significant differences were present among M1 and mutant structures in terms of average hydration number. Especially, M5 and M6 mutants, where a drift in the position of magnesium ions was observed, displayed a low hydration with respect to M1. The gain of function mutants M3 and M4, however, told a different story. In M3, the positions of hydrated sites were found to be slightly less with respect to M1. Specifically, the region around phosphate groups of residues A18/A19 and the highly hydrated sites around the sugar edges of residues G14/C15 were absent (Figure 7). This change indicated that an inversion G2C15 pair was affecting not only the NWC interaction with the A18 residue but also the arrangement of vicinal loop residues, which, in turn, led to an altered water
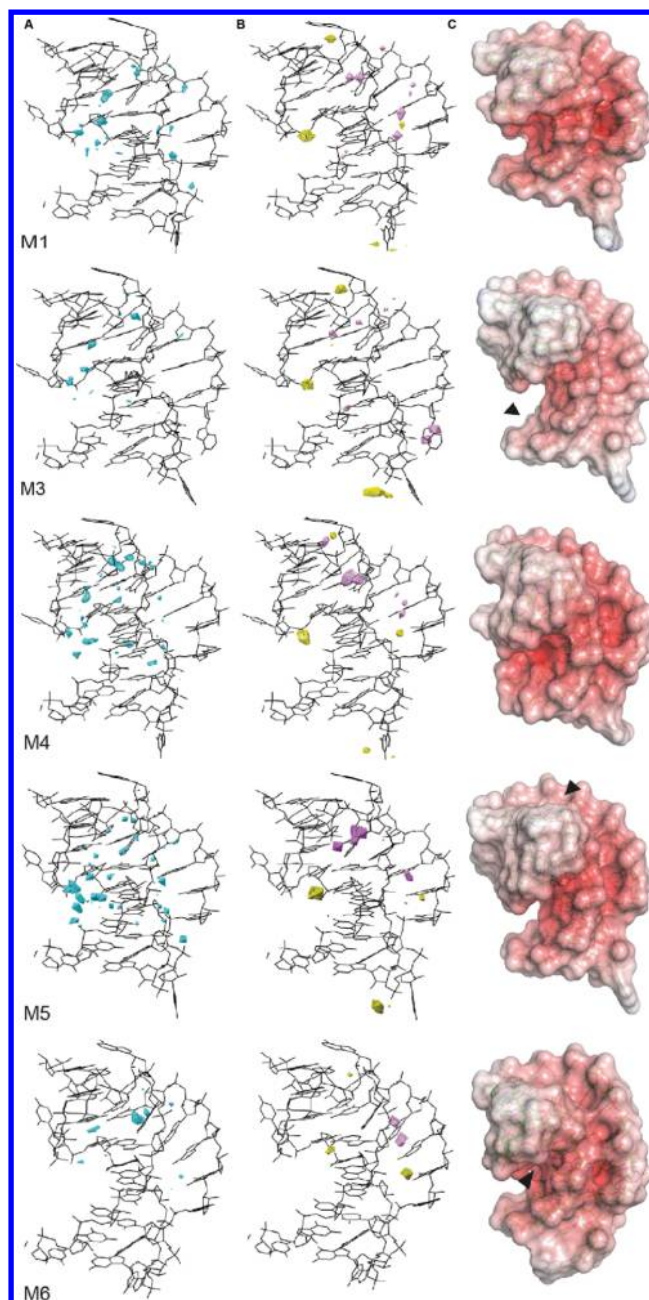

Figure 7. Hydration patterns of the average structures. (A) The water oxygen density is represented at a contour level of 334 hits (ten times bulk water density) per grid element (0.5 Å3) and is colored in turquoise mesh. (B) Sodium and magnesium ion densities are represented by purple and yellow meshes, respectively, at a contour level of 100 hits (three times bulk water density) per grid element (0.5 Å3). (C) Electrostatic potential surface (±25kT) is mapped on the last 10 ns average structures. Black arrowheads indicate positions in M3, M5, and M6 simulations, where a significant change in the electrostatic potential surface was observed.

arrangement at these sites (Figure 7, row 2). The most significant variation, however, was observed in the case of mutant M4. At 10× bulk water density, the total number of ordered hydration sites and hydration number was considerably more than that of the reference set (Figure 7). We observed a very strong density peak near the G5(O1P/O2P/O6/N7)−C6(N4)−G10(N4) group of atoms along with a pronounced peak near C6(2′−OH) and C23(N4) (Supplementary Table 5,

Table 3. Diffusion Constants of Magnesium Ions and Their Associated *B*-Factors

	B-factor[a]	D (10⁻⁵ cm²/s)						
ion type	X-ray	M1	M2	M3	M4	M5	M6	M7
Mg34	24.30	0.00074		−0.00442	0.01188	−0.00029	−0.00167	0.00081
Mg38	36.94	0.06937		0.00068	0.00495	0.99156	0.24002	0.00103
Mg45	41.40	0.00015		−0.00012	0.19307	0.20377	0.07417	0.03689
Mg52	53.29	0.19263		0.07517	0.05639	0.00030	0.04011	−0.00489

[a]*B*-factor values taken from the crystal structure.

Supporting Information, and Figure 6a, row 3). Relative to M1, the number of waters mediating hydrogen bonds in the minor groove face of residues C12, C13, and G14 and WC face of loop residues A19, C20, A21, and C23 increased in this case and hydration improved considerably at 10× water density (Figure 7A, row 3). Clearly, the presence of a C23 seemed to alter the local hydration patterns in and around interface of stems S1/S2 junction and L2/S2 region to a significant extent. An overall increase in the number of water-mediated and direct hydrogen bonds implicated toward a significantly compact and rigid pseudoknot conformation, which might pose a better ribosomal roadblock than its wild-type counterpart (M1), hence increasing −1 PRF efficiency.

On the contrary, the average hydration number in mutant M5 was less than M1 due to the loss of a small density peak near the phosphate oxygen of C8 and G9 residues and of a reduction in density near the major groove edges of C24, C25, and G26 residues in stem S2, due to absence of magnesium ion at this position (Figure 6A, row 4; Table 3). Apart from that, reduction in water densities between residue pairs C12/C13 and A7/C8 were observed in both the main and replicate sets of M5 trajectory at 10× density. It could be estimated from above observations that the loss of function in this mutant might arise due to a potential recognition between ribosome and stem S2, where optimum base pair geometries are maintained by resident ions and waters. An isosteric replacement of G5C12 by A5U12 in M6 caused the loss of consecutive N7 and O6 groups (of G4 and G5), which led to absence of bridging waters at this position. The loss of NWC interactions at the junction between A22/A5 resulted in an altered stacking arrangement between L2 residues ultimately leading to the loss of hydration sites in this region throughout the course of the trajectory. Although the number of waters mediating hydrogen bonds in M6 was slightly more than those in M1, the occupancies of these waters lasted only a few nanoseconds and fluctuated widely throughput the simulation.

Effect of Ions and Their Role in Stabilization of the Structure. We first investigated initial ionic positions as observed in the crystal structure (Supplementary Table 6 and Supplementary Figure S12, Supporting Information). Three magnesium ions were found to interact with RNA heavy atoms via coordinated water molecules,[37] albeit the role and significance of Mg38, sitting at the major groove face of S2, was not clear in the crystal structure studies. Mg34 was involved in a direct contact with the phosphate backbone of the G17 residue via electrostatic interactions. Mg45 and Mg52 were found to be located at the major groove of stem S1, interacting with consecutive G4/G5 and G2/C3 residues in the crystal structure, respectively. In addition to these magnesium ions, three sodium ions were found to be located at critical positions, mainly at the stem S1—loop L2 interface. To appreciate the change in the positioning of the ions across various simulation sets in a consequential way, we compared the electrostatic

potential surface with ionic density maps in different structures (Figure 7C). Visualization of ionic density maps at 3 times bulk water density led to some interesting observations. First, out of the four magnesium ions, Mg52 was clearly found to be inessential for maintaining structural integrity and stability. This was further corroborated by its high crystal *B*-factor value and high diffusivity in M1 simulation (Table 3). To eliminate any bias caused due to a high density cutoff used for displaying ionic density grid, a lowered cutoff value of 2 times that of bulk water was selected to visualize this density, but still no corresponding density for Mg52 could be located, in any of the conditions studied. Instead, we observed an alternate position of magnesium ion density near the backbone phosphate groups of A21 and G4 in M1, M4, M5, and M6 sets (Figure 7B). Contrary to this, Mg45, critically positioned at the base of S1 in its major groove, displayed high density peaks in M1, M3, M4, M5, and M7. In M6, this density was found to be lower as the presence of adenine (A5) introduced a −NH₂ group into the major groove, which resulted in lowering of negative potential at this position (Figure 7B, row 5). In M2, where we replaced all crystal magnesium with sodium ions, two small density peaks of sodium ions were observed lining the major groove edges of G4 and G5 residues. This site corresponded to the space occupied by Mg45 in wild-type structure (M1), indicating that sodium ions could effectively replace the magnesium without disturbing the structural integrity of the junction region of the BWYV pseudoknot. A similar trend was observed for Mg38, binding N7 and O6 of consecutive G25 and G26 of S2. In M2, the corresponding position for this ion was simultaneously occupied by two sodium ions (Supplementary Figure S11, Supporting Information). In M5, however, we did not observe any density for Mg38, as we replaced G25 with C25 leading to a loss of adjacent N7 and O6 groups of guanines. The large value of diffusion constant for Mg38 in M5 substantiated the loss of peak in the major groove of S2 (Table 3). Furthermore, the inversion of the C9G25 pair to the G9C25 pair in M5 led to an alteration in the electrostatic environment in the major groove of S2 (Figure 7C, row 4), eliminating the magnesium binding pocket from this region. Apart from M2 and M5, the location subscribing to the presence of Mg38 displayed a sharp high density ionic peak in remaining sets. This observation was further confirmed by the diffusivity values of Mg38 across different trajectories, highlighting the significance of this ion in the major groove of S2 (Table 3). Mg34, which forms a direct contact with the RNA backbone at G17, was found to be present at the same position in all sets except set M2, where we did not observe any ion density at the backbone of G17 residue (Supplementary Figure S11, Supporting Information). Despite the clear effect of the presence of magnesium ions on the pseudoknot as discussed above, the stability of this structure in terms of direct as well as water-mediated hydrogen bonds, in the absence of magnesium ions (M2) was comparable with the wild-type structure (M1).

This observation elucidates that magnesium ions *per se* play a less critical role in maintaining the global structure of the BWYV pseudoknot, because the sodium ion density was found at all the potential magnesium ion sites in M2, particularly at regions where multiple phosphate groups are juxtaposed to each other to generate highly electronegative patches. This is supported by the fact that within 40 ns of the simulation in M2 set, sodium ions lined themselves along the highly electronegative ridge formed by stem S1 and loop L2 (Supplementary Figure S11 and S13, Supporting Information).

Unlike magnesium ions, the densities observed for sodium ions were more sensitive to the structural changes introduced. As there was no bias in the initial placement of sodium ions in the structures, it was interesting for us to note that some sodiums actually moved to occupy the positions described by Egli et al.[37] in almost all the trajectories. The crossing of the stem S1 minor groove by loop L2 residues leads to formation of a "ridge and valley" like surface between S1 and L2 in the wild-type structure (M1), having almost uniform negative electrostatic potential (Figure 7, row 1 and Supplementary Figure S11, Supporting Information). In simulation set M7, after the flipping motion of cytosine C6, a sequential disruption of stacking among L2 residues A19−A23 was observed; this ultimately diminished the "ridge-valley" like surface and the associated negative potential (Supplementary Figure S11, Supporting Information). In the BWYV crystal structure, all of the sodium ions were located at this surface. Apparently, the sodium ion densities at this surface between S1 and L2 were markedly reduced in the M7 set when compared to the wild-type densities. This event was independent of the presence of magnesium ions in the structure.

■ CONCLUSIONS

The maintenance of a precise ratio of structural to functional proteins in many single-stranded RNA viruses depends on the efficiency of −1 PRF. A clear understanding of the −1 PRF process requires detailed information about structural differences between functional and nonfunctional forms of pseudoknots involved in ribosomal pausing. The involvement of an active role of pseudoknot in causing −1 PRF has been hinted at by various groups.[67−69] Our studies highlight this aspect from a structural perspective by dissecting the effects of various components, viz., ions, base-pair inversions in stems S1 and S2, and substitutions in loop regions on the structural integrity of the BWYV pseudoknot. The conformational dynamics of different gain and loss of function mutant structures reinforce the notion that −1 PRF is modulated by finer atomic level details of the pseudoknot, as none of the *in silico* mutations introduced affected the global fold of the pseudoknot adversely.

In M3, the inversion of pair G2C15 to C2G15 results in formation of new hydrogen bonds in the vicinity of G17 residue besides moderately affecting few water-mediated interactions. The 20% gain in efficiency in this mutant could be attributed to formation of these additional NWC hydrogen bonds. These additional hydrogen bonds could enhance the stability at the 5′-base of the pseudoknot and the inversion *per se* might lead to formation of alternate stable transition structures during unfolding/refolding of the structure. Mutant M4 (A23C), which reported a 200% gain in efficiency of −1 PRF, displayed major variations in almost all respects. This substitution profoundly affects NWC hydrogen bonds at the pseudoknot junction and overall hydration patterns of the structure. This

mutant closely resembles the junction geometry from ScYLV wild-type structure and displays a clear displacement of C6+ toward the G10C24 base pair. A reduced distance between C23 in L2 and C6+, leads to high occupancy of the hydrogen bond between C6+(O2)−C23(N4) and increases the correlated movements between residues at the junction region, viz., G5, C6+, C23, and G10. The two additional hydrogen bonds between A22:C23 and A7:C8 were a characteristic feature of this mutant, which were absent in native state simulations. A high density sodium ion peak was observed to lie near the backbone of C6+ in M4, which in turn, clustered a number of waters in this region.

The reason mutant M5 (C9G25 to G9C25) displayed a slight reduction in efficiency must arise from the reduced propeller twist and open angle observed for this S2 base pair. The inversion of a base pair in M5 leads to an altered base-pair configuration that might be responsible for the loss of putative recognition between incoming ribosome and nucleobases in S2. A cryo-EM map fitting of the 40s ribosome subunit reveals that ribosomal proteins surrounding the pseudoknot entry interface project multiple positively charged side chains that might form contacts with the incoming RNA structure. Furthermore, −1 PRF inducing pseudoknots from other viruses also shows large propeller twist values for this base pair. Additionally, the contiguity of N7 and O6 atoms in successive G25 and G26 is broken in this case, which ultimately led to a loss of magnesium ion binding site from major groove of S2. It might be possible that Mg38 is responsible for maintaining a specific geometry of C8C9 dinucleotide step more appropriate for ribosomal recognition and subsequent unfolding event. Simulation set M6 (G5C12 to A5U12), a complete loss of function mutant, displayed an expected behavior. Apart from absence of triplexes formed between A22:G5C12 and G5C12:A23 nucleotides, the neighboring triplex observed between G4C13 and A21 was also lost within 40 ns of the simulation. This structure had far less number of water-mediated interactions along with loss of critical Mg45 ion at the interface of the two stems. Simulation M7 revealed that N3-protonated cytosine C6+ in loop L1 plays a key role in stabilizing the geometry at the junction interface of the pseudoknot. The unprotonated C6 underwent a backbone torsional flip, moving away from C6−G10−C24 base platform. As C6+ forms water-mediated interaction with A23 residue in M1, the flipping motion in M7 disturbs this interaction. Hence, it progressively disturbs the geometry at the junction region, which results in larger fluctuation of L2 residues from A19 to A23. In these two cases, it became apparent that the geometry of residues in L2 was controlled by the NWC interactions in which these residues were involved. Once these interactions are lost, so is the geometry, which ultimately affects the conformation and function of the pseudoknot. In the absence of geometry stabilizing Mg38, a large and recurrent base-pair disruption for the C9G25 pair was observed in simulation M2, suggesting modulation of base-pair parameters by resident ions. However, as far as the number and type of WC/NWC hydrogen bonds and hydration sites were concerned, M2 closely mimicked the wild-type behavior, suggesting a less critical role of magnesium ion on the global pseudoknot conformation. Nearly all the sites occupied by sodium and magnesium ions in the crystal structure were found to be occupied by randomly added sodium ions in simulation M2, within 40 ns of the simulation.

This study highlights the reasons behind increase or decreases in the PRF inducing ability of pseudoknot and its

11917

dx.doi.org/10.1021/jp507154u | *J. Phys. Chem. B* 2014, 118, 11905−11920

mutants from BWYV. These observations can be extrapolated on similar pseudoknot structures involved in this process. The inferences drawn can be readily exploited to study unfolding kinetics and dynamics of both native and mutant PRF inducing pseudoknots either by means of single molecule experiments (using Atomic force microscopy) or by employing computational methods like steered molecular dynamics, to search for the presence of metastable transition states during unfolding pathway in these forms. These studies could involve either independent pseudoknot structures or pseudoknot structures modeled with ribosome, on mRNA entry tunnel, using cryo-EM maps as templates.

ASSOCIATED CONTENT

Ⓢ Supporting Information

Details of RMSD profiles of replicate sets and several additional analyses including base-pair geometry, DCCM, and stacking area overlap are given in supplementary files provided with this manuscript. Separate video files are also provided. This material is available free of charge via the Internet at http://pubs.acs.org.

AUTHOR INFORMATION

Corresponding Author

*M. Bansal. Tel: +91-80-22932534. Fax: +91-80-23600535. E-mail: mb@mbu.iisc.ernet.in.

Notes

The authors declare no competing financial interest.

ACKNOWLEDGMENTS

REFERENCES

(1) Staple, D. W.; Butcher, S. E. Pseudoknots: RNA Structures with Diverse Functions. *PLoS Biol.* **2005**, *3* (6), e213.

(2) Liu, B.; Mathews, D. H.; Turner, D. H. RNA Pseudoknots: Folding and Finding. *F1000 Biol. Rep* **2010**, *2*, 8.

(3) Dam, E.; Pleij, K.; Draper, D. Structural and Functional Aspects of RNA Pseudoknots. *Biochemistry* **1992**, *31* (47), 11665−76.

(4) Du, Z.; Giedroc, D. P.; Hoffman, D. W. Structure of the Autoregulatory Pseudoknot within the Gene 32 Messenger RNA of Bacteriophages T2 and T6: A Model for a Possible Family of Structurally Related RNA Pseudoknots. *Biochemistry* **1996**, *35* (13), 4187−98.

(5) Adams, P. L.; Stahley, M. R.; Gill, M. L.; Kosek, A. B.; Wang, J.; Strobel, S. A. Crystal Structure of a Group I Intron Splicing Intermediate. *RNA* **2004**, *10* (12), 1867−87.

(6) Asano, K.; Mizobuchi, K. An RNA Pseudoknot as the Molecular Switch for Translation of the Repz Gene Encoding the Replication Initiator of Incialpha Plasmid Colib-P9. *J. Biol. Chem.* **1998**, *273* (19), 11815−25.

(7) Leathers, V.; Tanguay, R.; Kobayashi, M.; Gallie, D. R. A Phylogenetically Conserved Sequence within Viral 3′ Untranslated RNA Pseudoknots Regulates Translation. *Mol. Cell. Biol.* **1993**, *13* (9), 5331−47.

(8) Schimmel, P. RNA Pseudoknots That Interact with Components of the Translation Apparatus. *Cell* **1989**, *58* (1), 9−12.

(9) Wang, C.; Le, S. Y.; Ali, N.; Siddiqui, A. An RNA Pseudoknot Is an Essential Structural Element of the Internal Ribosome Entry Site Located within the Hepatitis C Virus 5′ Noncoding Region. *RNA* **1995**, *1* (5), 526−37.

(10) Brierley, I.; Pennell, S.; Gilbert, R. J. Viral RNA Pseudoknots: Versatile Motifs in Gene Expression and Replication. *Nat. Rev. Microbiol.* **2007**, *5* (8), 598−610.

(11) ten Dam, E. B.; Pleij, C. W.; Bosch, L. RNA Pseudoknots: Translational Frameshifting and Readthrough on Viral Rnas. *Virus Genes* **1990**, *4* (2), 121−36.

(12) Brierley, I. Ribosomal Frameshifting Viral Rnas. *J. Gen. Virol.* **1995**, *76* (Pt 8), 1885−92.

(13) Huang, X.; Yang, Y.; Wang, G.; Cheng, Q.; Du, Z. Highly Conserved RNA Pseudoknots at the Gag-Pol Junction of Hiv-1 Suggest a Novel Mechanism of −1 Ribosomal Frameshifting. *RNA* **2014**, *20* (5), 587−93.

(14) Baranov, P. V.; Fayet, O.; Hendrix, R. W.; Atkins, J. F. Recoding in Bacteriophages and Bacterial Is Elements. *Trends Genet* **2006**, *22* (3), 174−81.

(15) Manktelow, E.; Shigemoto, K.; Brierley, I. Characterization of the Frameshift Signal of Edr, a Mammalian Example of Programmed −1 Ribosomal Frameshifting. *Nucleic Acids Res.* **2005**, *33* (5), 1553−63.

(16) Wills, N. M.; Moore, B.; Hammer, A.; Gesteland, R. F.; Atkins, J. F. A Functional −1 Ribosomal Frameshift Signal in the Human Paraneoplastic Ma3 Gene. *J. Biol. Chem.* **2006**, *281* (11), 7082−8.

(17) Clark, M. B.; Janicke, M.; Gottesbuhren, U.; Kleffmann, T.; Legge, M.; Poole, E. S.; Tate, W. P. Mammalian Gene Peg10 Expresses Two Reading Frames by High Efficiency −1 Frameshifting in Embryonic-Associated Tissues. *J. Biol. Chem.* **2007**, *282* (52), 37359−69.

(18) Tholstrup, J.; Oddershede, L. B.; Sorensen, M. A. mRNA Pseudoknot Structures Can Act as Ribosomal Roadblocks. *Nucleic Acids Res.* **2012**, *40* (1), 303−13.

(19) Jacks, T.; Madhani, H. D.; Masiarz, F. R.; Varmus, H. E. Signals for Ribosomal Frameshifting in the Rous Sarcoma Virus Gag-Pol Region. *Cell* **1988**, *55* (3), 447−58.

(20) Weiss, R. B.; Dunn, D. M.; Shuh, M.; Atkins, J. F.; Gesteland, R. F. E. Coli Ribosomes Re-Phase on Retroviral Frameshift Signals at Rates Ranging from 2 to 50%. *New Biol.* **1989**, *1* (2), 159−69.

(21) Baranov, P. V.; Gesteland, R. F.; Atkins, J. F. P-Site tRNA Is a Crucial Initiator of Ribosomal Frameshifting. *RNA* **2004**, *10* (2), 221−30.

(22) Chamorro, M.; Parkin, N.; Varmus, H. E. An RNA Pseudoknot and an Optimal Heptameric Shift Site Are Required for Highly Efficient Ribosomal Frameshifting on a Retroviral Messenger RNA. *Proc. Natl. Acad. Sci. U. S. A.* **1992**, *89* (2), 713−7.

(23) Brunelle, M. N.; Payant, C.; Lemay, G.; Brakier-Gingras, L. Expression of the Human Immunodeficiency Virus Frameshift Signal in a Bacterial Cell-Free System: Influence of an Interaction between the Ribosome and a Stem-Loop Structure Downstream from the Slippery Site. *Nucleic Acids Res.* **1999**, *27* (24), 4783−91.

(24) Giedroc, D. P.; Theimer, C. A.; Nixon, P. L. Structure, Stability and Function of RNA Pseudoknots Involved in Stimulating Ribosomal Frameshifting. *J. Mol. Biol.* **2000**, *298* (2), 167−85.

(25) Chen, G.; Chang, K. Y.; Chou, M. Y.; Bustamante, C.; Tinoco, I., Jr. Triplex Structures in an RNA Pseudoknot Enhance Mechanical Stability and Increase Efficiency of −1 Ribosomal Frameshifting. *Proc. Natl. Acad. Sci. U. S. A.* **2009**, *106* (31), 12706−11.

(26) Cao, S.; Chen, S. J. Predicting Ribosomal Frameshifting Efficiency. *Phys. Biol.* **2008**, *5* (1), 016002.

(27) Kontos, H.; Napthine, S.; Brierley, I. Ribosomal Pausing at a Frameshifter RNA Pseudoknot Is Sensitive to Reading Phase but Shows Little Correlation with Frameshift Efficiency. *Mol. Cell. Biol.* **2001**, *21* (24), 8657−70.

(28) Namy, O.; Moran, S. J.; Stuart, D. I.; Gilbert, R. J.; Brierley, I. A Mechanical Explanation of RNA Pseudoknot Function in Programmed Ribosomal Frameshifting. *Nature* **2006**, *441* (7090), 244−7.

(29) Plant, E. P.; Dinman, J. D. Torsional Restraint: A New Twist on Frameshifting Pseudoknots. *Nucleic Acids Res.* **2005**, *33* (6), 1825−33.

(30) Plant, E. P.; Jacobs, K. L.; Harger, J. W.; Meskauskas, A.; Jacobs, J. L.; Baxter, J. L.; Petrov, A. N.; Dinman, J. D. The 9-a Solution: How

mRNA Pseudoknots Promote Efficient Programmed −1 Ribosomal Frameshifting. *RNA* **2003**, *9* (2), 168−74.

(31) Harger, J. W.; Meskauskas, A.; Dinman, J. D. An "Integrated Model" of Programmed Ribosomal Frameshifting. *Trends Biochem. Sci.* **2002**, *27* (9), 448−54.

(32) Le, S. Y.; Chen, J. H.; Pattabiraman, N.; Maizel, J. V., Jr. Ion-RNA Interactions in the RNA Pseudoknot of a Ribosomal Frameshifting Site: Molecular Modeling Studies. *J. Biomol Struct Dyn* **1998**, *16* (1), 1−11.

(33) Csaszar, K.; Spackova, N.; Stefl, R.; Sponer, J.; Leontis, N. B. Molecular Dynamics of the Frame-Shifting Pseudoknot from Beet Western Yellows Virus: The Role of Non-Watson-Crick Base-Pairing, Ordered Hydration, Cation Binding and Base Mutations on Stability and Unfolding. *J. Mol. Biol.* **2001**, *313* (5), 1073−91.

(34) van Batenburg, F. H.; Gultyaev, A. P.; Pleij, C. W.; Ng, J.; Oliehoek, J. Pseudobase: A Database with RNA Pseudoknots. *Nucleic Acids Res.* **2000**, *28* (1), 201−4.

(35) Cornish, P. V.; Stammler, S. N.; Giedroc, D. P. The Global Structures of a Wild-Type and Poorly Functional Plant Luteoviral mRNA Pseudoknot Are Essentially Identical. *RNA* **2006**, *12* (11), 1959−69.

(36) Kim, Y. G.; Maas, S.; Wang, S. C.; Rich, A. Mutational Study Reveals That Tertiary Interactions Are Conserved in Ribosomal Frameshifting Pseudoknots of Two Luteoviruses. *RNA* **2000**, *6* (8), 1157−65.

(37) Egli, M.; Minasov, G.; Su, L.; Rich, A. Metal Ions and Flexibility in a Viral RNA Pseudoknot at Atomic Resolution. *Proc. Natl. Acad. Sci. U. S. A.* **2002**, *99* (7), 4302−7.

(38) Kim, Y. G.; Su, L.; Maas, S.; O'Neill, A.; Rich, A. Specific Mutations in a Viral RNA Pseudoknot Drastically Change Ribosomal Frameshifting Efficiency. *Proc. Natl. Acad. Sci. U. S. A.* **1999**, *96* (25), 14234−9.

(39) Lu, X.-J.; Olson, W. K. 3DNA: A Versatile, Integrated Software System for the Analysis, Rebuilding and Visualization of Three-Dimensional Nucleic-Acid Structures. *Nat. Protocols* **2008**, *3* (7), 1213−1227.

(40) Cornish, P. V.; Hennig, M.; Giedroc, D. P. A Loop 2 Cytidine-Stem 1 Minor Groove Interaction as a Positive Determinant for Pseudoknot-Stimulated −1 Ribosomal Frameshifting. *Proc. Natl. Acad. Sci. U. S. A.* **2005**, *102* (36), 12694−9.

(41) Rabl, J.; Leibundgut, M.; Ataide, S. F.; Haag, A.; Ban, N. Crystal Structure of the Eukaryotic 40s Ribosomal Subunit in Complex with Initiation Factor 1. *Science* **2011**, *331* (6018), 730−6.

(42) Liphardt, J.; Napthine, S.; Kontos, H.; Brierley, I. Evidence for an RNA Pseudoknot Loop-Helix Interaction Essential for Efficient −1 Ribosomal Frameshifting. *J. Mol. Biol.* **1999**, *288* (3), 321−35.

(43) Yusupova, G. Z.; Yusupov, M. M.; Cate, J. H.; Noller, H. F. The Path of Messenger RNA through the Ribosome. *Cell* **2001**, *106* (2), 233−41.

(44) Pearlman, D. A.; Case, D. A.; Caldwell, James W.; Ross, Wilson S.; Cheatham, Thomas E., III; DeBolt, Steve; Ferguson, David; Seibel, George; Kollman, P. Amber, a Package of Computer Programs for Applying Molecular Mechanics, Normal Mode Analysis, Molecular Dynamics and Free Energy Calculations to Simulate the Structural and Energetic Properties of Molecules. *Comput. Phys. Commun.* **1995**, *91*, 1−41.

(45) Aaqvist, J. Ion-Water Interaction Potentials Derived from Free Energy Perturbation Simulations. *J. Phys. Chem.* **1990**, *94* (21), 8021−8024.

(46) Jorgensen, W. L.; Chandrasekhar, J.; Madura, J. D.; Impey, R. W.; Klein, M. L. Comparison of Simple Potential Functions for Simulating Liquid Water. *J. Chem. Phys.* **1983**, *79* (2), 926−935.

(47) Allnér, O.; Nilsson, L.; Villa, A. Magnesium Ion−Water Coordination and Exchange in Biomolecular Simulations. *J. Chem. Theory Comput.* **2012**, *8* (4), 1493−1502.

(48) Veeraraghavan, N.; Bevilacqua, P. C.; Hammes-Schiffer, S. Long-Distance Communication in the HDV Ribozyme: Insights from Molecular Dynamics and Experiments. *J. Mol. Biol.* **2010**, *402* (1), 278−291.

(49) Frisch, M. J.; Trucks, G. W.; Schlegel, H. B.; Scuseria, G. E.; Robb, M. A.; Cheeseman, J. R.; Scalmani, G.; Barone, V.; Mennucci, B.; Petersson, G. A.; et al. *Gaussian 09*, Revision B.01; Gaussian Inc.: Wallingford, CT, 2009.

(50) Cieplak, P.; Cornell, W. D.; Bayly, C.; Kollman, P. A. Application of the Multimolecule and Multiconformational Resp Methodology to Biopolymers: Charge Derivation for DNA, RNA, and Proteins. *J. Comput. Chem.* **1995**, *16* (11), 1357−1377.

(51) Dupradeau, F. Y.; Pigache, A.; Zaffran, T.; Savineau, C.; Lelong, R.; Grivel, N.; Lelong, D.; Rosanski, W.; Cieplak, P. The R.E.D. Tools: Advances in Resp and Esp Charge Derivation and Force Field Library Building. *Phys. Chem. Chem. Phys.* **2010**, *12* (28), 7821−39.

(52) Darden, T.; York, D.; Pedersen, L. Particle Mesh Ewald - an N.Log(N) Method for Ewald Sums in Large Systems. *J. Chem. Phys.* **1993**, *98* (12), 10089−10092.

(53) Essmann, U.; Perera, L.; Berkowitz, M. L.; Darden, T.; Lee, H.; Pedersen, L. G. A Smooth Particle Mesh Ewald Method. *J. Chem. Phys.* **1995**, *103* (19), 8577−8593.

(54) Marathe, A.; Bansal, M. The 5-Methyl Group in Thymine Dynamically Influences the Structure of a-Tracts in DNA at the Local and Global Level. *J. Phys. Chem. B* **2010**, *114* (16), 5534−46.

(55) Madhumalar, A.; Bansal, M. Structural Insights into the Effect of Hydration and Ions on a-Tract DNA: A Molecular Dynamics Study. *Biophys. J.* **2003**, *85* (3), 1805−16.

(56) Pettersen, E. F.; Goddard, T. D.; Huang, C. C.; Couch, G. S.; Greenblatt, D. M.; Meng, E. C.; Ferrin, T. E. UCSF Chimera–a Visualization System for Exploratory Research and Analysis. *J. Comput. Chem.* **2004**, *25* (13), 1605−12.

(57) Bansal, M.; Bhattacharyya, D.; Ravi, B. NUPARM and NUCGEN: Software for Analysis and Generation of Sequence Dependent Nucleic Acid Structures. *Comput. Appl. Biosci* **1995**, *11* (3), 281−7.

(58) Leontis, N. B.; Westhof, E. Geometric Nomenclature and Classification of RNA Base Pairs. *RNA* **2001**, *7* (4), 499−512.

(59) McDonald, I. K.; Thornton, J. M. Satisfying Hydrogen Bonding Potential in Proteins. *J. Mol. Biol.* **1994**, *238* (5), 777−93.

(60) Baker, N. A.; Sept, D.; Joseph, S.; Holst, M. J.; McCammon, J. A. Electrostatics of Nanosystems: Application to Microtubules and the Ribosome. *Proc. Natl. Acad. Sci. U. S. A.* **2001**, *98* (18), 10037−41.

(61) Caulfield, T. R.; Devkota, B.; Rollins, G. C., Examinations of tRNA Range of Motion Using Simulations of Cryo-EM Microscopy and X-Ray Data. *J. Biophys.* **2011**, *2011*.

(62) Su, L.; Chen, L.; Egli, M.; Berger, J. M.; Rich, A. Minor Groove RNA Triplex in the Crystal Structure of a Ribosomal Frameshifting Viral Pseudoknot. *Nat. Struct. Biol.* **1999**, *6* (3), 285−92.

(63) Pallan, P. S.; Marshall, W. S.; Harp, J.; Jewett, F. C., 3rd; Wawrzak, Z.; Brown, B. A., 2nd; Rich, A.; Egli, M. Crystal Structure of a Luteoviral RNA Pseudoknot and Model for a Minimal Ribosomal Frameshifting Motif. *Biochemistry* **2005**, *44* (34), 11315−22.

(64) Shen, L. X.; Tinoco, I., Jr. The Structure of an RNA Pseudoknot That Causes Efficient Frameshifting in Mouse Mammary Tumor Virus. *J. Mol. Biol.* **1995**, *247* (5), 963−78.

(65) Michiels, P. J.; Versleijen, A. A.; Verlaan, P. W.; Pleij, C. W.; Hilbers, C. W.; Heus, H. A. Solution Structure of the Pseudoknot of Srv-1 RNA, Involved in Ribosomal Frameshifting. *J. Mol. Biol.* **2001**, *310* (5), 1109−23.

(66) Napthine, S.; Liphardt, J.; Bloys, A.; Routledge, S.; Brierley, I. The Role of RNA Pseudoknot Stem 1 Length in the Promotion of Efficient −1 Ribosomal Frameshifting. *J. Mol. Biol.* **1999**, *288* (3), 305−20.

(67) Chen, X.; Chamorro, M.; Lee, S. I.; Shen, L. X.; Hines, J. V.; Tinoco, I., Jr.; Varmus, H. E. Structural and Functional Studies of Retroviral RNA Pseudoknots Involved in Ribosomal Frameshifting: Nucleotides at the Junction of the Two Stems Are Important for Efficient Ribosomal Frameshifting. *EMBO J.* **1995**, *14* (4), 842−52.

(68) Chen, X.; Kang, H.; Shen, L. X.; Chamorro, M.; Varmus, H. E.; Tinoco, I., Jr. A Characteristic Bent Conformation of RNA Pseudoknots Promotes −1 Frameshifting During Translation of Retroviral RNA. *J. Mol. Biol.* **1996**, *260* (4), 479−83.

(69) Ritchie, D. B.; Foster, D. A.; Woodside, M. T. Programmed −1 Frameshifting Efficiency Correlates with RNA Pseudoknot Conformational Plasticity, Not Resistance to Mechanical Unfolding. *Proc. Natl. Acad. Sci. U. S. A.* **2012**, *109* (40), 16167−72.